Atomistic modeling of LiF microstructure ionic conductivity and its influence on nucleation and plating

Lorena Alzate-Vargas, K. S. N. Vikrant, Srikanth Allu, and Jean-Luc Fattebert

Phys. Rev. Materials **6**, 095402 — Published 9 September 2022

DOI: 10.1103/PhysRevMaterials.6.095402

Atomistic modelling of LiF microstructure ionic conductivity and its influence on nucleation and plating

Lorena Alzate-Vargas,* K. S. N. Vikrant, Srikanth Allu, and Jean-Luc Fattebert
Computational Sciences and Engineering Division,
Oak Ridge National Laboratory
Oak Ridge, TN, USA

The formation and degradation of the solid electrolyte interphase (SEI) and its underlying transport properties play an essential role in the overall performance of lithium-ion batteries. This article presents classical molecular dynamics studies on polycrystalline inorganic lithium fluoride (LiF) layers to model and predict the SEI transport properties. The ionic conductivity is obtained from the lithium-ion diffusivity in polycrystalline structures of LiF using the Nernst-Einstein relation. The predicted molecular dynamics data is used in a continuum scale phase-field model to evaluate the plating kinetics under fast charging conditions. The analysis emphasizes that the SEI ionic conductivity properties impact the plating dynamics, where SEI's low ion conductivity value is prone to large plating and subsequent capacity degradation. The combination of atomic and continuum scale studies shown herein lays a foundation to tune in SEI transport properties to decrease the amount of lithium plating and improve the performance of fast-charging batteries.

I. INTRODUCTION

The solid electrolyte interphase (SEI) layer that forms on the surface of the anode during initial charging cycles of a Li-ion battery is an important component that critically affects the performance of a battery, preventing further electrolyte reduction. Despite extensive efforts in experimental techniques, recently focusing on silicon anodes (see for instance [1]), the SEI structure and composition are not fully characterized. In a general consensus on the heterogeneity and multicomponent structure of the SEI, it is believed to be formed by an organic-rich layer and an inorganic inner layer close to the electrode, generally consisting of LiF, Li_2CO_3 and Li_2O [2–4].

Atomic simulations such as molecular dynamics (MD) have been used in recent years to complement experiments and give a detailed picture of the SEI composition, morphology and thickness [5–7]. While these efforts have not yet led to a fully formed SEI microstructure, model SEI systems based on experimental information can be proposed to reveal the structure-property relationships by predicting relevant material properties.

Experimental results indicate that the multicomponent SEI is rather a polycrystalline material with grain boundaries (GBs) and heterogeneous interfaces. As the SEI grows, ion transport mechanisms can be significantly affected by these heterogeneities, especially GBs and material composition. Understanding the relations between structure and properties of the SEI can help to increase the cycling performance of Li-ion batteries.

Simulations can give insights on the lithium transport properties through the SEI layer. Multiple studies on diffusion of Li^+ in SEI individual components (or SEI as single crystals) have been reported in the literature. When studying Li-ion diffusion in Li_2CO_3 from density functional theory (DFT) simulations, Shi et al. [8] concluded that the main Li^+ transport mechanism was via knock-off. Using classical MD simulations, Benitez et al. [9] studied Li^+ diffusion in a single crystal structure for three inorganic materials commonly associated with the SEI. Their simulations revealing different diffusion mechanisms for each material, a vacancy-assisted and knock-off diffusion in LiF and Li_2CO_3, and direct ion-exchange mechanism in Li_2O. From these studies, it appears that transport behavior is specific to each SEI component.

To account for the fact that the SEI is a polycrystalline structure, theories describing ion transport via porous regions, via grain boundaries between the SEI components or via interstitials and vacancies have been advanced, as ionic conduction across the SEI can significantly impact the rate capability of the battery. Experimental diffusion coefficients of the heterostructured SEI have been reported from electrochemical impedance spectroscopy analysis.[10] However, experimental data is limited since characterization on diffusion and conductivity across the SEI is a difficult task that requires precise and specifically designed tools. Few recent modeling works have started to assess the role of GBs in Li ion transport in SEI. For example, Ramasubramanian et al. [11] used DFT calculations to study the Li-ion diffusion coefficients and dominant pathways through the polycrystalline SEI (Li_2O and LiF) formed by two grain boundaries. Their results indicate that Li diffusion through the homogeneous LiF/LiF GB is faster or comparable to that of a pure grain, but slower than in heterogeneous LiF/Li_2O GB. In the context of solid electrolytes, Heo et al. [12] combined small MD simulations (including disordered ones) with a mesoscopic phase-field model to calculate effective ionic conductivities in a polycrystal. Dawson et al. [13] used MD to calculate Li-ion conductivity for specific grain boundary angles, the values were used in combination with single crystal values to estimate an effective conductivity.

Though several independent studies have been con-

* alzatevargll@ornl.gov

ducted to understand the SEI passivation and stability in presence of the electrolyte, the influence of this heterogeneous micro-structure on intercalation dynamics and ion transport in electrode particles is rarely analyzed. We believe the physical phenomenon at the interface between the SEI and electrode is relevant, especially during fast charging conditions where lithium, due to inherent thermodynamic limitations, could nucleate and start plating.

Pseudo-2D models are used to predict the SEI layer thickness based on irreversible formation reaction growth rate equations [14, 15]. Due to its resistance, SEI transport properties add an additional potential loss across the interface [15]. The new SEI layer formation growth on fresh cracks was modeled by several authors [16, 17]. Lithium plating has been considered as an important degradation mechanism under low temperatures or large current loadings [15, 18, 19]. These methods are average predictions of degradation of lithium-ion single cells due to loss of lithium inventory in these side reactions. Several authors proposed continuum models to evolve the local metallic lithium nucleation and growth for specific conditions [20–23]. Experimental in-situ methods have been developed to characterize the plated lithium at the full electrode scale and localized plating using imaging and diffraction techniques [24–30]. Despite all the efforts, there is a lack of understanding on the influence of SEI transport properties on lithium plating for fast charging batteries.

In this paper, we report an explicit calculation of Li-ion conductivity through a microstructure using all-atom MD simulations to determine the effect of ion transport on lithium plating. As a first step towards modeling Li^+ diffusion through a polycrystalline material, we assume an SEI composed of LiF only. LiF is one recurring material that is present in nearly all functional SEIs with conventional carbonate electrolytes [31, 32]. It has been found that fluorinating the SEI with LiF can improve the cycling performance of Li metal anode based batteries [33]. MD simulations of polycrystalline LiF are used to calculate ionic conductivity while identifying that GBs contribute mainly to the overall transport properties. However, as we will show in this paper, it can be a challenging problem from a computational point of view. This is mainly due to the slow diffusion process in LiF at room temperature, that requires long time-scales for accurate calculations.

The result from atomistic simulations is used subsequently to parameterize a nucleation and plating phase-field model that incorporates interfacial reactions associated with intercalation and plating. The study allows us to evaluate the effects of the SEI transport properties on lithium nucleation and plating on graphite electrodes for fast charging batteries, which lays a foundation to tune in SEI properties to reduce the amount of lithium plating.

II. METHODS

A. Molecular dynamics simulations

We use the open source software Atomsk [34] to generate three LiF polycrystal samples with randomly oriented grains using Voronoi tesselations from a LiF rock-salt crystal structure: (i) one sample with volume $10\times10\times10$ nm^3 and eight packed grains, (ii) a second sample with the same volume ($10\times10\times10$ nm^3) but containing 64 random LiF grains, and (iii) a larger system with volume $15\times15\times15$ nm^3 volume and eight grains. Given the completely random orientations of the grains, we do not expect any special grain boundary and no matching of the adjacent crystal lattices.

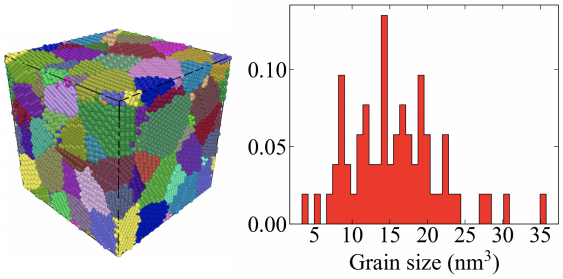

FIG. 1: Initial configuration of LiF polycrystal containing 64 grains in a $(10\ nm)^3$ volume and its grain size distribution.

After construction of the polycrystals, some atoms in the GBs are located in close proximity to each other. Before running MD simulations, ions separated by a distance less than 2.0 Å– the LiF crystal lattice parameter — were removed upfront while charge neutrality was maintained. Figure 1 shows the initial configuration of a polycrystal containing 64 grains and its grain size distribution, displaying the wide variety of grains available in the sample. In Appendix A, extra details about the eight grains polycrystal models can be found. This approach is very similar to the one use by Dawson et al. [35] to model Na-ion conductivity in sulfide and oxide solid electrolytes.

Lithium fluoride atomic interactions are modeled with a standard 6–12 Lennard-Jones potential energy and long-range electrostatic interactions were described using a Coulomb potential both with cutoff distance of 12 Å. The potential parameters for Li^+ and F^- were obtained from Ref. [36], following the Lorentz-Berthelot combination rules, and were proved effective to study LiF crystal diffusion in MD [9]. OVITO [37] is used to visualize and identify atomic structures.

All molecular dynamics simulations were performed using the LAMMPS code [38]. MD runs of 20 ns were completed using a time step of 1 fs. Simulations were carried out at 300 K using the NVT ensemble with a Nose-Hoover thermostat. Before production runs, each

system was annealed at 500 K for 250 ps and then cooled down to 300 K at a rate of 3 K/ps. This is mostly to remove artifacts from the generation of the initial structure, specifically at the grain boundaries, and not to mimic to the process that lead to these microstructure formation *in-situ* during which we do not expect any high temperature annealing. Self-diffusion data for Li were obtained from an MSD analysis according to

$$D_i = \frac{1}{6t}\langle |r_i(t) - r_i(0)|^2 \rangle \tag{1}$$

for t =20 ns. Where $\langle . \rangle$ denotes the average over all atoms of species i. Long simulations like this (10 ns or more) were required due to the slow diffusivity in this polycrystal system. Note that this has also been deemed necessary to study ionic liquids [39] where diffusivity is also slow.

Ionic conductivity can be calculated via the Nernst-Einstein method based on the ion self-diffusion coefficients during the last 10 ns. Yet, it is well known that this relationship neglects ion cross-correlation effects resulting in upper estimates of the conductivity. A more precise approach would be to use MD perturbation theory and Green-Kubo formalism to directly evaluate ionic conductivity. Our numerical investigation showed however that for the system of interest here, the signal-to-noise ratio is too small to achieve meaningful conclusions. This is mostly due to the small conductivity value being measured in our calculations, in comparison to commonly measured values using the Green-Kubo approach such as liquid electrolytes [40]. Given these considerations, we estimated that the Nernst-Einstein relationship given in Equation 2 would give us a better estimate of conductivity,

$$\sigma_{\mathrm{NE}} = \frac{e^2 N}{k_B T V} \sum_i z_i^2 D_i \tag{2}$$

where N is the total number of atoms, V the volume, e is the charge of an electron, z_i is the ion charge, and D_i is the self-diffusion coefficient for each component i in the system.

B. Continuum Modeling

The influence of SEI inhomogeneities on plating kinetics is studied by introducing the LiF SEI transport properties in the earlier developed phase field model [41, 42]. Here, the SEI is modeled as a non-evolving phase with interfacial reactions. During nucleation, lithium nuclei volume fraction is created at the expense of the non-conserved electrolyte and SEI phases. This approach indirectly accounts for SEI fracture, allowing for lithium metal to be exposed to the electrolyte. The underlying assumptions include constant values for the SEI conductivity and SEI equilibrium potential, independent of Li-ion concentration.

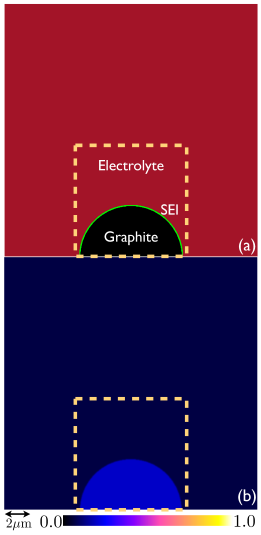

FIG. 2: A single particle simulation setup for understanding the effect of SEI conductivity on the plating kinetics under fast charge conditions: (a) schematic of electrolyte region (red), SEI (green), and anode graphite particle (black), (b) corresponding initial lithium concentration in electrolyte, SEI and graphite regions. In color bar, 1 represents fully lithiated state of graphite and 0 is complete delithiated state of graphite. Highlighted dashed box shows a magnified region used in results (see Section III B).

Following the recent modeling of lithium plating kinetics on graphite particles under fast charging conditions [42], four regions defined by phase-field order parameters ($\{\xi_i\} = \xi_l, \xi_e, \xi_a, \xi_{sei}$) with a site fraction rule: $\xi_l + \xi_e + \xi_a + \xi_{sei} = 1$ were used. Here, $\xi_l = 1$ represents the metallic lithium region, $\xi_e = 1$ the electrolyte region, $\xi_a = 1$ the anode region, and $\xi_{sei} = 1$ the SEI region. An order parameter with value 0 means that the corresponding phase is not existent at that location in the simulation domain. A value between 0 and 1 corresponds to an interfacial region. Additionally, we use c to represent the concentration of lithium species, having a valence of Z and molar volume ω.

The total free energy functional of the given electrochemical system, G is:

$$\begin{aligned} G[\{\xi_i\}, c, \rho; T] = \int_\Omega \Big[& g(\{\xi_i\}, c, T) + \tfrac{\alpha_l}{2} (\nabla \xi_l)^2 \\ & + \tfrac{\alpha_e}{2} (\nabla \xi_e)^2 + \tfrac{\alpha_a}{2} (\nabla \xi_a)^2 + \tfrac{\alpha_{sei}}{2} (\nabla \xi_{sei})^2 + \\ & \tfrac{\alpha_c}{2} (\nabla c)^2 + \rho \phi \Big] d\Omega \end{aligned} \tag{3}$$

where g is the Gibbs free energy density, α_l, α_e, α_a, α_{sei} are the gradient energy coefficients of the different interfaces, and α_c is a chemical species penalty coefficient for the phase separation. ρ is the electrostatic charge density, ϕ is the voltage, and Ω is the total volume.

The time evolution equation for the metallic lithium phase ξ_l follows an Allen-Cahn equation [43] with an ad-

ditional non-variational term, an interfacial plating reaction flux, $\vec{\Gamma}_{pla}$ through the anode surface, which results in:

$$\frac{\partial \xi_l}{\partial t} = -M_{\xi_l}\left[\frac{\partial g}{\partial \xi_l} - \alpha_l \nabla^2 \xi_l - \frac{\alpha_a}{2}\nabla^2 \xi_a\right] + \omega \vec{\Gamma}_{pla} \cdot \nabla \xi_a \tag{4}$$

Here, M_{ξ_l} is the Allen-Cahn mobility of ξ_l.

The order parameter associated with the anode region, ξ_a does not evolve in time and is considered as an heterogeneous substrate. ξ_{sei} and ξ_e do not have time dependent equations, however, as it grows, the evolved ξ_l replaces the localized volume of ξ_{sei} and ξ_e in the current formulation.

The lithium concentration evolves according to a Cahn-Hilliard equation [44] and similar to magnesium plating [45] with two additional non-variational terms: (i) an interfacial plating reaction flux $\vec{\Gamma}_{pla}$ through the anode surface, which model the conversion of lithium ions at the anode interface into a metal phase and reverse, and (ii) an intercalation reaction flux $\vec{\Gamma}_{int}$ through the anode surface accounting for intercalation of lithium in graphite during charging and de-intercalation during discharging. The resulting time-evolution equation for the lithium ions species is given by

$$\begin{aligned} \frac{\partial c}{\partial t} &= \nabla \cdot M \nabla \left[\frac{\partial g}{\partial c} + \frac{Z\mathcal{F}}{\omega}\phi\right] - \nabla \cdot M \alpha_c \nabla^3 c \\ &\quad -\omega \vec{\Gamma}_{pla} \cdot \nabla \xi_a + \omega \vec{\Gamma}_{int} \cdot \nabla \xi_a \end{aligned} \tag{5}$$

where, M is a mobility parameter for the lithium ions concentration, and $\mathcal{F}$ is Faraday's constant.

In addition, an equation for the electrostatic potential ϕ is obtained from a charge-continuity equation with the associated phases and chemical components [41, 42].

$$\begin{aligned} 0 &= \nabla \cdot \kappa \nabla \phi + \frac{\mathcal{F} Z c}{\omega}(\nabla \cdot M \nabla [\frac{\partial g}{\partial c}] - \nabla \cdot M \alpha_c \nabla^3 c) \\ &\quad -Z\mathcal{F}\vec{\Gamma}_{pla} \cdot \nabla \xi_a + Z\mathcal{F}\vec{\Gamma}_{int} \cdot \nabla \xi_a \end{aligned} \tag{6}$$

Equation (6) represents the charge transport kinetics, where the spatial conductivity is given by $\kappa = \kappa_l p(\xi_l) + \kappa_e p(\xi_e) + \kappa_a p(\xi_a) + \kappa_{sei} p(\xi_{sei})$. Here, $\kappa_l, \kappa_e, \kappa_a, \kappa_{sei}$ are the conductivities of metallic lithium, electrolyte, anode and SEI respectively, and $p(\xi_i) = \xi_i^3(6\xi_i^2 - 15\xi_i + 10)$ is an interpolation function. The SEI conductivity value, κ_{sei}, is obtained from MD simulations in this work. All the physical properties and detailed set of equations used in the model are presented in the Appendix B.

The initial setup used to study the effect of SEI on plating kinetics under fast charge conditions is shown in Figure 2(a). A 2D domain (20μm$\times 20\mu$m) consisting of three different regions: electrolyte $\xi_e = 1$ (red), an anode graphite particle $\xi_a = 1$ of 8μm diameter(black), and a 200 nm thick SEI layer $\xi_{sei} = 1$ (green). The corresponding initial mole fraction of lithium is shown in Figure 2(b). A silver color is used to represent plated metallic lithium in the manuscript. The mesh used for the setup is uniform with 500×500 elements. The bottom edge is grounded with $\phi = 0$ and a constant flux boundary condition is applied at the top edge (current/C-Rate). The set of order parameters, ξ_i, and concentration field, c have zero flux boundary condition on all sides. Equations (4)–(6) are implemented using the FiPy solver [46] using a LinearPCGSolver with a relative tolerance for convergence set to 1×10^{-8} at every time step of Δt=5 s.

In the current model, the nucleation of metallic lithium was introduced at sites on anode graphite surface with the minimum local plating potential below 0 V, conceptually in agreement with the experimental studies [47]. The critical radius of lithium nucleus, $r_c = -\frac{2\gamma_{l,sei}\omega_j}{Z\mathcal{F}\eta_{pla}+\Delta g_f \omega_j}$, is a function of local plating overpotential, η_{pla}, surface energy of metallic lithium/SEI, $\gamma_{l,sei}$, and bulk free energy of transformation, Δg_f. The numerical limitation of minimum radius to be resolved is 0.1 μm with at least five elements, few nanometers below the continuity nucleation theory is not valid.

III. RESULTS AND DISCUSSION

A. Diffusion and conductivity values of LiF

We quantify the Li-ion conduction properties through the self-diffusion coefficient of Li-ion in LiF calculated using the mean square displacements (MSD) obtained from the MD trajectory as shown in Figure 1.

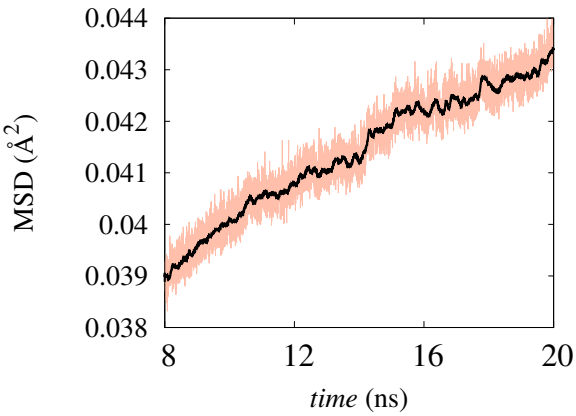

FIG. 3: Li mean square displacement in a $15 \times 15 \times 15$ nm^3 LiF system with eight grains at 300 K from 8 to 20 ns. Running average every 100 steps shown as black line.

From our simulations, we estimate that Li-ion diffusivity in polycrystal LiF is between 10^{-14} and 10^{-15} m^2/s (see Table I). Our values are higher than the lithium ion diffusion value of 4.6×10^{-16} m^2/s reported for a LiF/LiF grain boundary, [11] but comparable with the lithium diffusivity in a Li_2CO_3/LiF interface [48] at 300 K calculated as 7.6×10^{-15} m^2/s.

As described in Section II A, we calculated the ionic conductivity for the polycrystalline samples using the Nernst-Einstein equation. Our computed ionic conduc-

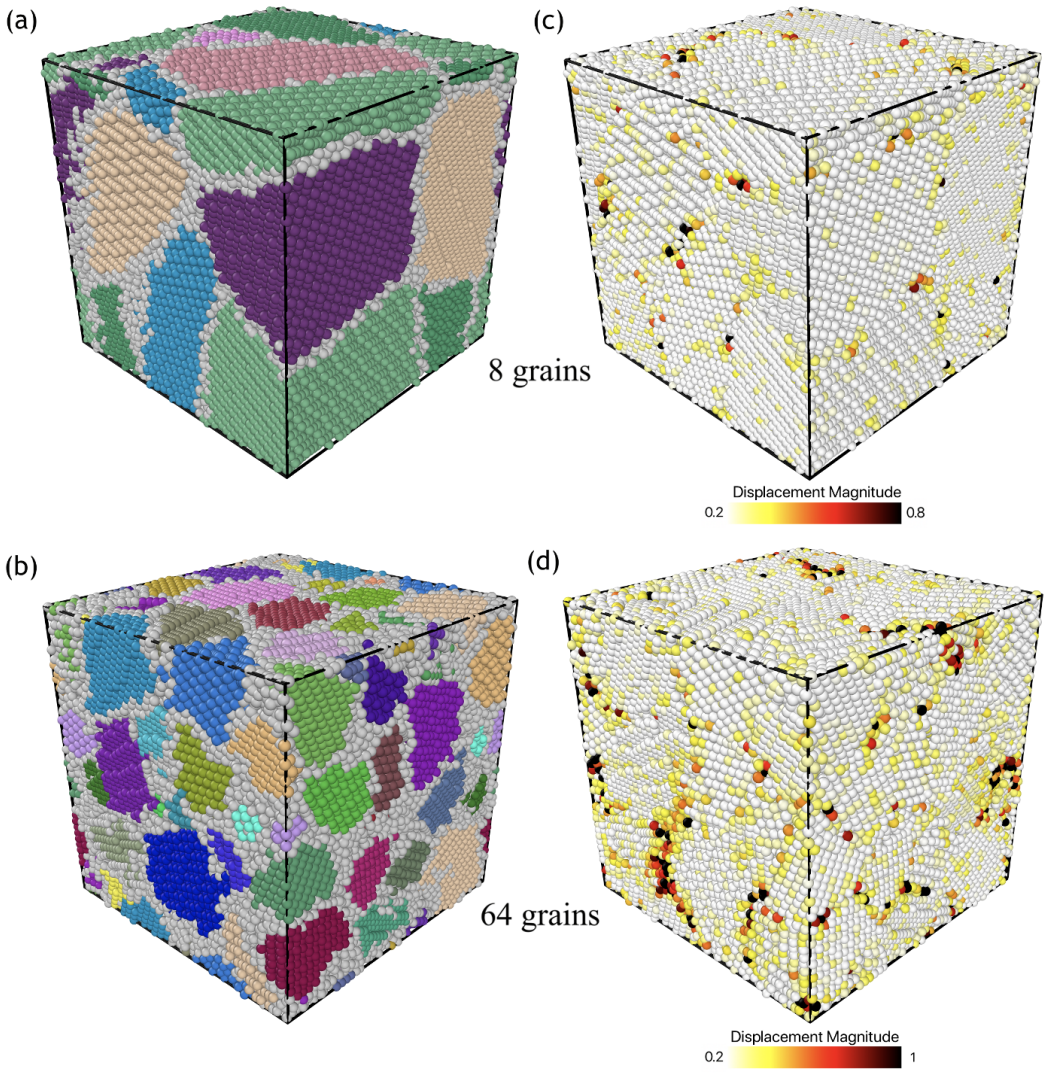

FIG. 4: Local ordering and atomic displacement in $(10\ \text{nm})^3$ polycrystal samples. (a)-(b) Grain identification based on coordination for 8 and 64 grains respectively. Atoms identified as grain boundaries are colored in gray and bulk atoms are colored by grain. (c)-(d) Color map of atomic displacement magnitude taken at 20 ns of MD run for 8 and 64 grain samples respectively. Displacement magnitude color bar has been adjusted for better visualization, where white represents almost zero ion mobility.

tivities are about 10^{-5} S/cm for all samples, larger magnitudes seem to be associated with the smaller grains (see Table I).

TABLE I: Lithium diffusion and conductivity values measured by MD in three LiF poly crystalline samples.

Size (nm)	No. Grains	D_{Li} (m^2/s)	σ_{Li} (S/cm)
10	8	6.1×10^{-15}	2.1×10^{-5}
10	64	1.1×10^{-14}	3.7×10^{-5}
15	8	3.3×10^{-15}	1.2×10^{-5}

To better understand how diffusion is affected by GB, radial distribution functions can be used to analyze differences between bulk and polycrystal samples [35]. In contrast, we measured the atomic displacements for all Li-ions in the system and correlate these with the local atomic ordering. Local ordering can be obtained from a coordination analysis that calculates the number of nearest neighbors for each atom. Fully coordinated lattice atoms have all the same number of nearest neighbors, while atoms that belong to GBs are usually miscoordinated [37]. Grain atom identification analysis is shown in Figure 4(a) and Figure 4(b) for two systems with different numbers of grains, eight and 64 grains respectively. Bulk atoms, whose nearest neighbor atoms match simple cubic crystal lattice, are colored according to the grain they belong to, whereas gray atoms in both

figures represent atoms identified as non-ordered, therefore classified as grain boundaries.

We calculate the Li-ion displacement magnitude at 20 ns, since displacement is related to diffusion by the Einstein relation described in Equation 1. Each Li-ion is colored based on their displacement magnitudes as can be seen in Figures 4(c) and 4(d), where white colored atoms display minimum, almost zero displacement from the initial configuration and red to black atoms are associated with most mobile ions in the system. Across all three polycrystal systems, we observe visually that larger atomic displacement magnitudes tend to correspond with ions matching the grain boundaries. As diffusion and ionic conductivity are higher in the system with 64 grains, we observe that a larger fraction of mobile ions are present than in the eight grain sample.

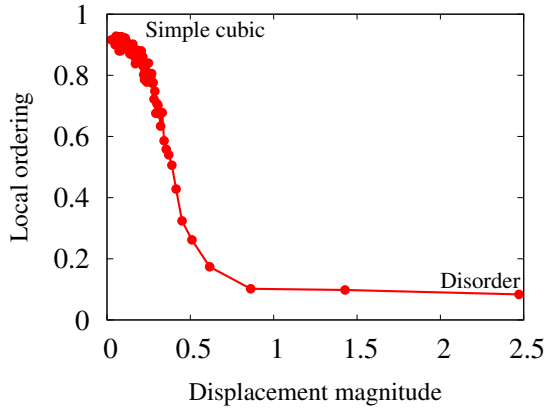

FIG. 5: Correlation between Li ion displacement magnitude and atomic local ordering as obtained from snapshot at the end of the 20 ns simulation in $(10\text{nm})^3$ sample with 8 grains. Atomic displacements values were sorted before being groups into bins of 500. Data points plotted in this figure show the average order versus the average displacement for each bin. Local ordering ranges from 0 — meaning disorder atomic structure — to 1 — identified as simple cubic lattice.

To confirm our initial visual analysis that larger displacements correspond to grain boundary atoms, we carry out the following quantitative analysis: (i) the displacements of all the lithium ions in each system were sorted and atoms were binned according to their magnitude, (ii) the local ordering of each atom being characterized as 0 or 1 for disordered atoms and bulk atoms respectively, an average order was computed for each bin, (iii) the averaged local ordering was plotted as a function of average displacement magnitude for each bin. Results are displayed in Figure 5 for the eight grains sample. It can be seen that the atoms with minimum displacement magnitude are primarily identified as bulk atoms, i.e. simple cubic structure, whereas disordered atoms have larger displacements. This strong correlation between local disorder and displacements indicates an enhanced diffusion across interfaces and grain boundaries rather than through the bulk.

B. Continuum Scale Modeling Results

Lithium nucleation and plating mechanism on anode is diffusion-limited in the graphite or electrolyte [20, 49, 50]. Here, bulk diffusion and conductivity of SEI and graphite determine the thermodynamic criteria of nucleation of metallic lithium. The κ_{sei}, conductivity calculations obtained from MD simulations in Section III A is subsequently used for continuum simulations (see Figure 2). The analysis below highlights the effect of SEI conductivity on the plating kinetics under fast charge conditions.

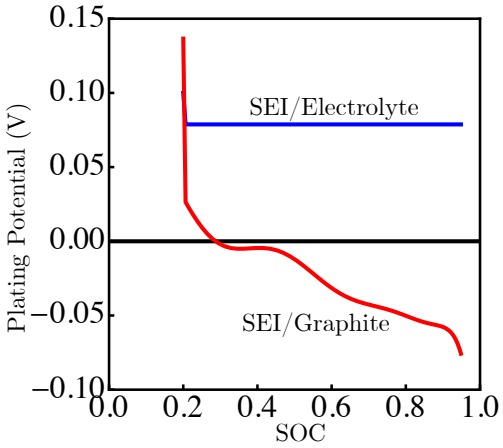

FIG. 6: Predicted average plating overpotential at graphite/SEI and SEI/electrolyte interface for 4C-Rate charging.

Figure 6 shows the plating potential at the graphite/SEI and SEI/electrolyte interfaces. This means the change in electrostatic potential, ϕ, from equilibrium across the interface, as a function of State of Charge (SOC) for a 4C charging condition. At the SEI/electrolyte interface (see blue curve) the thermodynamic limit for plating potential is almost constant and does not vary with any increase with SOC because the equilibrium potential of SEI is assumed to be constant and independent of SOC. At the SEI/graphite interface (see red curve) the thermodynamic limit for plating potential initial drops due to polarization losses and goes below zero for high SOC values. The analysis emphasizes that lithium nucleation happens at the graphite/SEI interface, where the plating overpotential is less than zero. At the SEI/electrolyte interface, the nucleation event is thermodynamically not favored under fast charge conditions.

Figure 7 shows the influence of SEI on lithium plating kinetics under a 4C-rate charging condition. Figure 7(a) show the lithium nucleation and plating in the absence of SEI (modeled by removing the ξ_{sei} phase). An iso-

lated nuclei and clusters of few nuclei coalescence is observed. In the presence of SEI, the low ion conductivity of SEI induces a large negative plating potential at graphite/SEI interface, compared to graphite/electrolyte interface. The large negative plating potential at a large number of sites allows for nucleation and subsequent lithium plating growth, resulting in a strip of platted lithium on the graphite surface (see Figure 7(b)). This illustrates how the SEI ionic conductivity properties have an influence on the plating kinetics, where the low conductivity value results in platted lithium which wets the graphite/electrolyte interface.

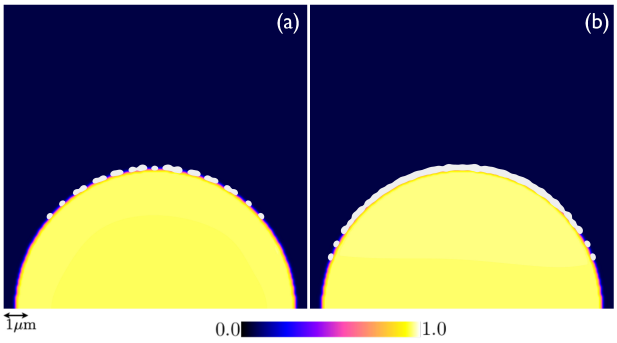

FIG. 7: Simulated metallic lithium nucleation and plating kinetics under a charging condition for 4C-Rate. (a) no SEI influence, (b) SEI influence. Color scheme is the same as used in Fig. 2

A parametric analysis of the SEI ionic conductivity is shown in Figure 8 in order to understand the SOC condition for the onset of metallic lithium nucleation for various C-Rates. At low SEI conductivity, i.e., $\kappa_{sei} < \kappa_e$ (see red line), nucleation does not happen below 1C and more nucleation is favorable at low SOC, i.e., ~ 0.3 for C-Rates above 4.0. For $\kappa_{sei} > \kappa_e$ (see blue line), nucleation does not happen below 4C and gradually the threshold SOC for nucleation increases for different C-Rates from the previous two cases, with increase in C-Rate. Overall, an SEI with lower ionic conductivity than the electrolyte thermodynamically favors more nucleation sites and kinetically results in larger amount of plating compared to the large ionic conductivity values. This parametric analysis indicates that if an SEI with a higher ionic conductivity can be formed via experiments, it could suppress the lithium plating and loss of lithium inventory.

IV. CONCLUDING REMARKS

Continuum scale models of lithium ion batteries (LIB), like many other continuum models, rely on multiple materials parameters. The knowledge of these parameters can critically affect the accuracy of a model and the properties we want to quantify. Materials parameters are often not directly measurable by in-situ experiments, and thus atomistic models can be very useful in extending and

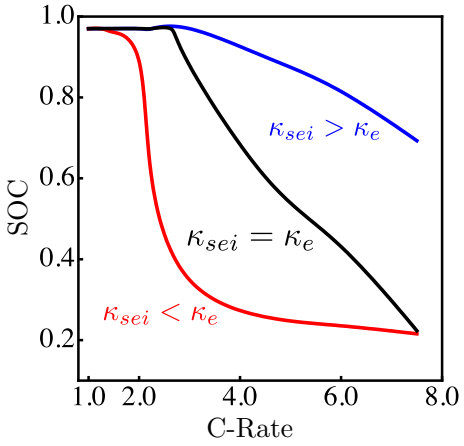

FIG. 8: SOC of the graphite anode for the onset of lithium nucleation on graphite as function of C-Rate for three SEI conductivity values: 1.5×10^{-3} S/m (red line), 0.64 S/m (black line), 6.4 S/m (blue line).

refining these parameters. In this paper, we quantified the lithium ions diffusion and conductivity parameters through the SEI via atomic-scale simulations. We then use that parameter value in a phase-field model of three phases (anode + SEI + electrolyte), to model the growth of a fourth phase, lithium metal, responsible for lithium plating. We demonstrate the benefit of combining predictive simulations at multiple length scales to gain better insight into the physical phenomena of lithium plating.

We choose that our three polycrystal models are characterised by (i) being made of grains large enough to be stable and, (ii) being small enough to allow equilibration in a reasonable time-to-solution scale. Characteristics, such as grain sizes and number of GBs, show the diversity of GBs in these samples. Extracting statistical information beyond what we presented here is likely to be very computationally demanding. For such an endeavor, we believe a multiscale model such as the one proposed by Heo et al. [12] would likely be more appropriate. Potentially such multiscale model could be parameterized using our MD data instead of two separate sets of independent bulk and disordered data.

Research on LIB is a very active field. While our simulations highlight the importance of SEI conductivity and its impact on nucleation and plating, they also further emphasize the importance of better characterizing the SEI in general [51]. Further progress is likely to come out of both experiments and computer simulations, from interactions between researchers in these two fields, and from agreements and discrepancies between their results. Computer models have their limitations, often due to computational complexity, and approximations have to be kept in mind when analysing results. On the other hand, experiments also have their limits, in particular when it comes to in situ measurements in LIB.

For instance, ionic conductivity on ex situ LiF SEI

were recently obtained from experimental characterization and estimated to be about 10^{-9} S/cm [52], several orders of magnitude smaller than the results from this work. However, the values presented in Tab. I, which range from 1.2×10^{-5} to 3.7×10^{-5} S/m, are consistent with other theoretical works [9, 11, 53] where reported diffusion coefficients and ionic conductivities are about one order of magnitude lower than ours. Values of same order of magnitude as ours are also used in continuum scale models [54]. Given the more disordered nature of our GBs, we expect our estimate to be indeed higher than predicted values for single crystal or special GBs. Also, according to Heo et al. multiscale model [12], a decrease in conductivity of almost an order of magnitude can be expected when grain sizes vary from 5 nm, typical size in our simulations, to 50 nm — grain size measured in Ref. [52], explaining part of the discrepancy. To explain the remaining discrepancy, based on our model and other theoretical models, we can speculate that the experimental microstructure reported in [52] may be characterized by a higher proportion of special GBs, with specific values of misorientation, which allow atoms from neighbouring lattices to coincide, — more resistant to ionic conductivity, a possible output from the deposition process used to form these microstructures. It points to a fundamental question about SEI: what type of GBs are present in these microstructures?. Lacking nanoscale details of GBs in SEI, and given the nature of the SEI microstructure and its formation, we believe our random polycrystal model is a good choice to start exploring conductivity in this type of systems.

It should be noted that the accuracy of our numerical results could possibly be improved by using more refined atomic potentials such as machine learning (ML) potentials as implemented for molten LiF systems [55, 56]. However these could be challenging at low temperature regimes when long time scale simulations are required. In addition, the results of Lam et al. [55] seem to indicate that these ML potentials lead to very similar diffusion coefficients as classical force-field, at least for high temperatures.

Yet, our approach proves very valuable in understanding the effect of the conductivity on lithium plating and can be extended to other SEI compositions and microstructures.

ACKNOWLEDGMENTS

This work is supported by the U.S. Department of Energy Vehicle Technologies Office and was carried out at Oak Ridge National Laboratory under Contract No. DE-AC05-00OR22725 with UT Battelle, LLC. This research used resources of the Compute and Data Environment for Science at the Oak Ridge National Laboratory, which is supported by the Office of Science of the U.S. Department of Energy under Contract No. DE-AC05-00OR22725.

Appendix A: Polycrystal models

TABLE II: Volumes and number of faces for each grain in the (10 nm)^3 and (15 nm)^3 polycrystal systems with eight grains

	10 nm		15 nm	
Grain	Volume ($\times10^5$ nm^3)	No. Faces	Volume ($\times10^5$ nm^3)	No. Faces
1	1.51	17	3.42	11
2	1.60	24	5.22	19
3	1.58	19	5.14	20
4	1.20	16	5.88	21
5	1.20	15	5.14	20
6	0.88	13	3.06	16
7	1.19	15	4.63	17
8	0.83	11	3.51	17

Appendix B: Continuum model details

The Gibbs free energy density, g is:

$$g(\{\xi_i\},c,T) = \frac{1}{\omega}\Big(g_c(\xi_l,\xi_e,\xi_a,\xi_{sei},T)c + k_bTc\ln[c] + k_bT(1-c)\ln[1-c] + g_c^{ex}(\xi_l,\xi_e,\xi_a,\xi_{sei},T)\Big) + \sum_{i\neq j}^{\{\xi\}} w_{ij}h(\xi_i,\xi_j)$$

The formation energy of Li^+ ionic species is defined as

$$g_c(\xi_l,\xi_e,\xi_a,\xi_{sei},T) = g_c^l(T)p(\xi_l) + g_c^e(T)p(\xi_e) + g_c^a(T)p(\xi_a) + g_c^{sei}(T)p(\xi_{sei})$$

where g_c^l, g_c^e, g_c^a, g_c^{sei} corresponds to formation energies of (Li^+) ionic species in lithium metal, electrolyte, anode graphite, and SEI regions respectively, and

$$g_c^{ex}(\xi_l,\xi_e,\xi_a,\xi_{sei},T) = g_c^{l,ex}(T)p(\xi_l) + g_c^{e,ex}(T)p(\xi_e) + g_c^{a,ex}(T)p(\xi_a) + g_c^{sei,ex}(T)p(\xi_{sei})$$

where $g_c^{l,ex}$, $g_c^{e,ex}$, $g_c^{a,ex}$, $g_c^{sei,ex}$ corresponds to excess energies of (Li^+) ionic species in lithium metal, electrolyte, anode graphite, and SEI regions respectively.

The pair wise interaction (double well potential) is defined as $h(\xi_i,\xi_j) = \xi_i^2\xi_j^2$ and w_{ij} is the corresponding energy barrier height for each ij-interface, with i,j=l,e,a,sei. We use $w_{ij} = \frac{3\gamma_{ij}}{\delta}$. The terms δ and γ_{ij} correspond to the thickness and interfacial energies of the ij-th interface.

The molar volume of the (Li^+) ionic species is defined as $\omega = \omega^l p(\xi_l) + \omega^e p(\xi_e) + \omega^a p(\xi_a) + \omega^{sei} p(\xi_{sei})$, where ω^l, ω^e, ω^a, ω^{sei} corresponds to molar volume of lithium metal, electrolyte, anode graphite, and SEI regions. R is

universal gas constant, T is temperature.

The intercalation reaction, $\vec{\Gamma}_{int}$ at the anode surface,

$$\vec{\Gamma}_{int} = j_{\circ,int}\Big(\exp[(1-\alpha_{int})(\frac{Z\mathcal{F}\eta_{int}}{RT} + \frac{\gamma_{int}\mathcal{K}\omega_j}{RT})] - \exp[-\alpha_{int}(\frac{Z\mathcal{F}\eta_{int}}{RT} + \frac{\gamma_{int}\mathcal{K}\omega}{RT})]\Big)\hat{n}$$

$j_{\circ,int} = \frac{i_{\circ,int}}{Z\mathcal{F}}$ is the intercalation molar exchange current density, $i_{\circ,int}$ is intercalation exchange current density, $\hat{n} = -\frac{\nabla\xi_a}{|\nabla\xi_a|}$ is the interface outward normal, $\mathcal{K} = \nabla\cdot\hat{n}$ is the curvature, γ_{int} is the interfacial energy, and $\alpha_{int} = 0.5$ is cathodic charge transfer coefficient for intercalation reaction.

The intercalation overpotential [57] is defined as $\eta_{int} = \Delta\phi - \Delta\phi_{g,\circ} = \frac{1}{Z\mathcal{F}}\frac{\delta G}{\delta c}$.

The difference in voltage across the interface is $\Delta\phi$, and the open circuit voltage at equilibrium is $\Delta\phi_{g,\circ}$.

The lithium plating reaction rate is,

$$\vec{\Gamma}_{pla} = j_{\circ,pla}\Big(\exp[(1-\alpha_{pla})(\frac{Z\mathcal{F}\eta_{pla}}{RT} + \frac{\gamma_{int}\mathcal{K}\omega}{RT})] - \exp[-\alpha_{pla}(\frac{Z\mathcal{F}\eta_{pla}}{RT} + \frac{\gamma_{int}\mathcal{K}\omega}{RT})]\Big)\hat{n}$$

$j_{\circ,pla} = \frac{i_{\circ,pla}}{Z\mathcal{F}}$ is the lithium plating molar exchange current density, $i_{\circ,pla}$ is exchange current density, and $\alpha_{pla} = 0.7$ is cathodic charge transfer coefficient for plating, and $\eta_{pla} = \Delta\phi - \Delta\phi_{Li,\circ}$ is the local overpotential for lithium plating on electrolyte/graphite interface, where $\Delta\phi_{Li,\circ} = 0$ is the equilibrium potential of lithium metal [29, 41, 58, 59].

TABLE III: Summary of physical parameters used in the continuum scale model

Symbol	Value	Units	Ref.
g_c^l	0	J/m^3	[60]
g_c^e	-2.746×10^{-6}	J/m^3	[60, 61]
g_c^a	-2.28×10^{-5}	J/m^3	[62]
$g_c^{a,ex}$	-57001.6c + 616.208c^2 − 4.84246 × 10$^6c^3$ + 2.37793 × 10$^7c^4$ − 7.4 × 10$^7c^5$ + 1.47689 × 10$^8c^6$ − 1.88177 × 10$^8c^7$ + 1.47969 × 10$^8c^8$ − 6.54345 × 10$^7c^9$ + 1.2452 × 10$^7c^{10}$	J/mol	[63, 64]
γ_{le}	1.73	J/m^2	[65]
γ_{ea}	0.035	J/m^2	[29]
γ_{al}	1.73	J/m^2	–
γ_{lsei}, γ_{esei}, γ_{asei}	1.73	J/m^2	–
γ_{asei}	1.73	J/m^2	–
δ	8×10^{-8}	m	[66]
w_{le}	0.65×10^8	J/m^3	[43, 67]
w_{ea}	0.013×10^8	J/m^3	[43, 67]
w_{al}	0.65×10^8	J/m^3	[43, 67]
w_{lsei}	0.65×10^8	J/m^3	[43, 67]
w_{esei}	0.013×10^8	J/m^3	[43, 67]
w_{asei}	0.65×10^8	J/m^3	[43, 67]
α_l	8.3×10^{-7}	J/m	[43, 67]
α_a	1.68×10^{-8}	J/m	[43, 67]
α_e	1.68×10^{-8}	J/m	[43, 67]
α_{sei}	1.68×10^{-8}	J/m	[43, 67]
α_c	$10^{-6}p(\xi_a)$	J/m	–
$i_{\circ,int}$	$0.4((0.001c_e/\omega_e)^{0.5})\times((0.001c/\omega_g)^{0.5})\times((0.001(1.0-c)/\omega_g)^{0.5})$	A/m^2	[29]
$i_{\circ,pla}$	10	A/m^2	[68]
ω^l	1.3×10^{-5}	m^3/mol	[65]
ω^a	3.23×10^{-5}	m^3/mol	[29]
ω^e	6.93×10^{-5}	m^3/mol	[29, 66]
ω^{sei}	6.93×10^{-5}	m^3/mol	–
κ^l	10^7	S/m	[29]
κ^a	100	S/m	[29]
κ^e	0.6426	S/m	[29]
D_j^g	3×10^{-14}	m^2/s	[29]
M_{ξ_l}	10^{-12}	m^3/Js	–

[1] Y. Xu, K. Wood, J. Coyle, C. Engtrakul, G. Teeter, C. Stoldt, A. Burrell, and A. Zakutayev, Chemistry of electrolyte reduction on lithium silicide, The Journal of

Physical Chemistry C **123**, 13219 (2019).
[2] M. Nie, D. Chalasani, D. P. Abraham, Y. Chen, A. Bose, and B. L. Lucht, Lithium ion battery graphite solid electrolyte interphase revealed by microscopy and spectroscopy, The Journal of Physical Chemistry C **117**, 1257 (2013).
[3] E. Peledand S. Menkin, Review—SEI: Past, present and future, Journal of The Electrochemical Society **164**, A1703 (2017).
[4] Y. Zhou, M. Su, X. Yu, Y. Zhang, J.-G. Wang, X. Ren, R. Cao, W. Xu, D. R. Baer, Y. Du, O. Borodin, Y. Wang, X.-L. Wang, K. Xu, Z. Xu, C. Wang, and Z. Zhu, Real-time mass spectrometric characterization of the solid–electrolyte interphase of a lithium-ion battery, Nature Nanotechnology **15**, 224 (2020).
[5] N. Takenaka, Y. Suzuki, H. Sakai, and M. Nagaoka, On electrolyte-dependent formation of solid electrolyte interphase film in lithium-ion batteries: Strong sensitivity to small structural difference of electrolyte molecules, The Journal of Physical Chemistry C **118**, 10874 (2014).
[6] L. Alzate-Vargas, S. M. Blau, E. W. C. Spotte-Smith, S. Allu, K. A. Persson, and J.-L. Fattebert, Insight into SEI growth in li-ion batteries using molecular dynamics and accelerated chemical reactions, The Journal of Physical Chemistry C **125**, 18588 (2021).
[7] J. W. Abbottand F. Hanke, Kinetically corrected Monte Carlo–molecular dynamics simulations of solid electrolyte interphase growth, Journal of Chemical Theory and Computation **18**, 925 (2022).
[8] S. Shi, P. Lu, Z. Liu, Y. Qi, L. G. Hector, H. Li, and S. J. Harris, Direct calculation of li-ion transport in the solid electrolyte interphase, Journal of the American Chemical Society **134**, 15476 (2012).
[9] L. Benitezand J. M. Seminario, Ion Diffusivity through the Solid Electrolyte Interphase in Lithium-Ion Batteries, Journal of The Electrochemical Society **164**, E3159 (2017).
[10] A. Churikov, Transfer mechanism in solid-electrolyte layers on lithium: influence of temperature and polarization, Electrochimica acta **46**, 2415 (2001).
[11] A. Ramasubramanian, V. Yurkiv, T. Foroozan, M. Ragone, R. Shahbazian-Yassar, and F. Mashayek, Lithium Diffusion Mechanism through Solid-Electrolyte Interphase in Rechargeable Lithium Batteries, Journal of Physical Chemistry C **123**, 10237 (2019).
[12] T. W. Heo, A. Grieder, B. Wang, M. Wood, T. Hsu, S. A. Akhade, L. F. Wan, L.-Q. Chen, N. Adelstein, and B. C. Wood, Microstructural impacts on ionic conductivity of oxide solid electrolytes from a combined atomistic-mesoscale approach, npj Computational Materials **7**, 214 (2021).
[13] J. A. Dawson, P. Canepa, T. Famprikis, C. Masquelier, and M. S. Islam, Atomic-scale influence of grain boundaries on li-ion conduction in solid electrolytes for all-solid-state batteries, Journal of the American Chemical Society **140**, 362 (2018).
[14] P. Verma, P. Maire, and P. Novák, A review of the features and analyses of the solid electrolyte interphase in Li-ion batteries, Electrochimica Acta **55**, 6332 (2010).
[15] J. M. Reniers, G. Mulder, and D. A. Howey, Review and Performance Comparison of Mechanical-Chemical Degradation Models for Lithium-Ion Batteries, Journal of The Electrochemical Society **166**, A3189 (2019).
[16] I. Laresgoiti, S. Käbitz, M. Ecker, and D. U. Sauer, Modeling mechanical degradation in lithium ion batteries during cycling: Solid electrolyte interphase fracture, Journal of Power Sources **300**, 112 (2015).
[17] A. Wang, S. Kadam, H. Li, S. Shi, and Y. Qi, Review on modeling of the anode solid electrolyte interphase (SEI) for lithium-ion batteries, npj Computational Materials **4**, 1 (2018).
[18] S. J. Harris, A. Timmons, D. R. Baker, and C. Monroe, Direct in situ measurements of Li transport in Li-ion battery negative electrodes, Chemical Physics Letters **485**, 265 (2010).
[19] A. M. Colclasure, A. R. Dunlop, S. E. Trask, B. J. Polzin, A. N. Jansen, and K. Smith, Requirements for Enabling Extreme Fast Charging of High Energy Density Li-Ion Cells while Avoiding Lithium Plating, Journal of The Electrochemical Society **166**, A1412 (2019).
[20] P. Arora, M. Doyle, and R. E. White, Mathematical Modeling of the Lithium Deposition Overcharge Reaction in Lithium-Ion Batteries Using Carbon-Based Negative Electrodes, Journal of The Electrochemical Society **146**, 3543 (1999).
[21] M. H. Tang, P. Albertus, and J. Newman, Two-Dimensional Modeling of Lithium Deposition during Cell Charging, ECS Meeting Abstracts **MA2008-02**, 1290 (2008).
[22] S. Tippmann, D. Walper, L. Balboa, B. Spier, and W. G. Bessler, Low-temperature charging of lithium-ion cells part I: Electrochemical modeling and experimental investigation of degradation behavior, Journal of Power Sources **252**, 305 (2014).
[23] X. G. Yang, Y. Leng, G. Zhang, S. Ge, and C. Y. Wang, Modeling of lithium plating induced aging of lithium-ion batteries: Transition from linear to nonlinear aging, Journal of Power Sources **360**, 28 (2017).
[24] M. C. Smartand B. V. Ratnakumar, Effects of Electrolyte Composition on Lithium Plating in Lithium-Ion Cells, Journal of The Electrochemical Society **158**, A379 (2011).
[25] M. Petzl, M. Kasper, and M. A. Danzer, Lithium plating in a commercial lithium-ion battery - A low-temperature aging study, Journal of Power Sources **275**, 799 (2015).
[26] C. von Lüders, V. Zinth, S. V. Erhard, P. J. Osswald, M. Hofmann, R. Gilles, and A. Jossen, Lithium plating in lithium-ion batteries investigated by voltage relaxation and in situ neutron diffraction, Journal of Power Sources **342**, 17 (2017).
[27] T. Waldmann, B. I. Hogg, and M. Wohlfahrt-Mehrens, Li plating as unwanted side reaction in commercial Li-ion cells – a review, Journal of Power Sources **384**, 107 (2018).
[28] C. Shen, G. Hu, L. Z. Cheong, S. Huang, J. G. Zhang, and D. Wang, Direct Observation of the Growth of Lithium Dendrites on Graphite Anodes by Operando EC-AFM, Small Methods **2**, 1700298 (2018).
[29] E. J. McShane, E. J. McShane, A. M. Colclasure, D. E. Brown, D. E. Brown, Z. M. Konz, Z. M. Konz, K. Smith, B. D. McCloskey, and B. D. McCloskey, Quantification of Inactive Lithium and Solid-Electrolyte Interphase Species on Graphite Electrodes after Fast Charging, ACS Energy Letters **5**, 2045 (2020).
[30] P. P. Paul, E. J. McShane, A. M. Colclasure, N. Balsara, D. E. Brown, C. Cao, B. R. Chen, P. R. Chinnam, Y. Cui, E. J. Dufek, D. P. Finegan, S. Gillard, W. Huang, Z. M. Konz, R. Kostecki, F. Liu, S. Lubner, R. Prasher, M. B.

Preefer, J. Qian, M. T. F. Rodrigues, M. Schnabel, S. B. Son, V. Srinivasan, H. G. Steinrück, T. R. Tanim, M. F. Toney, W. Tong, F. Usseglio-Viretta, J. Wan, M. Yusuf, B. D. McCloskey, and J. Nelson Weker, A review of existing and emerging methods for lithium detection and characterization in Li-ion and Li-metal batteries, Advanced Energy Materials **11**, 2100372 (2021).

[31] J. Tan, J. Matz, P. Dong, J. Shen, and M. Ye, A growing appreciation for the role of lif in the solid electrolyte interphase, Advanced Energy Materials **11**, 2100046 (2021).

[32] J. Chen, X. Fan, Q. Li, H. Yang, M. R. Khoshi, Y. Xu, S. Hwang, L. Chen, X. Ji, C. Yang, H. He, C. Wang, E. Garfunkel, D. Su, O. Borodin, and C. Wang, Electrolyte design for LiF-rich solid–electrolyte interfaces to enable high-performance microsized alloy anodes for batteries, Nature Energy **5**, 386 (2020).

[33] R. Pathak, K. Chen, A. Gurung, K. M. Reza, B. Bahrami, J. Pokharel, A. Baniya, W. He, F. Wu, Y. Zhou, K. Xu, and Q. Q. Qiao, Fluorinated hybrid solid-electrolyte-interphase for dendrite-free lithium deposition, Nature Communications **11**, 93 (2020).

[34] P. Hirel, Atomsk: A tool for manipulating and converting atomic data files, Computer Physics Communications **197**, 212 (2015).

[35] J. A. Dawson, P. Canepa, M. J. Clarke, T. Famprikis, D. Ghosh, and M. S. Islam, Toward understanding the different influences of grain boundaries on ion transport in sulfide and oxide solid electrolytes, Chemistry of Materials **31**, 5296 (2019).

[36] A. H. Maoand R. V. Pappu, Crystal lattice properties fully determine short-range interaction parameters for alkali and halide ions, The Journal of Chemical Physics **137**, 064104 (2012).

[37] A. Stukowski, Visualization and analysis of atomistic simulation data with OVITO the open visualization tool, Modeling and Simulation in Materials Science and Engineering **18**, 10.1088/0965-0393/18/1/015012 (2010).

[38] A. P. Thompson, H. M. Aktulga, R. Berger, D. S. Bolintineanu, W. M. Brown, P. S. Crozier, P. J. in 't Veld, A. Kohlmeyer, S. G. Moore, T. D. Nguyen, R. Shan, M. J. Stevens, J. Tranchida, C. Trott, and S. J. Plimpton, LAMMPS - a flexible simulation tool for particle-based materials modeling at the atomic, meso, and continuum scales, Computer Physics Communications **271**, 108171 (2022).

[39] M. Klähnand A. Seduraman, What determines CO2 solubility in ionic liquids? a molecular simulation study, The Journal of Physical Chemistry B **119**, 10066 (2015).

[40] T. Hou, K. D. Fong, J. Wang, and K. A. Persson, The solvation structure, transport properties and reduction behavior of carbonate-based electrolytes of lithium-ion batteries, Chem. Sci. **12**, 14740 (2021).

[41] K. S. N. Vikrantand S. Allu, Modeling of Lithium Nucleation and Plating Kinetics Under Fast Charge Conditions, Journal of The Electrochemical Society **168**, 020536 (2021).

[42] K. S. N. Vikrant, E. McShane, A. M. Colclasure, B. D. McCloskey, and S. Allu, Quantification of Dead Lithium on Graphite Anode under Fast Charging Conditions, Journal of The Electrochemical Society **169**, 040520 (2022).

[43] W. J. Boettinger, J. A. Warren, C. Beckermann, and A. Karma, Phase-field simulation of solidification, Annual Review of Materials Science **32**, 163 (2002).

[44] J. W. Cahn, Free energy of a nonuniform system. II. Thermodynamic basis, The Journal of Chemical Physics **30**, 1121 (1959).

[45] S. DeWitt, N. Hahn, K. Zavadil, and K. Thornton, Computational Examination of Orientation-Dependent Morphological Evolution during the Electrodeposition and Electrodissolution of Magnesium, Journal of The Electrochemical Society **163**, A513 (2015).

[46] J. E. Guyer, D. Wheeler, and J. A. Warren, FiPy: Partial differential equations with python, Computing in Science and Engineering **11**, 6 (2009).

[47] Y. Chen, K. H. Chen, A. J. Sanchez, E. Kazyak, V. Goel, Y. Gorlin, J. Christensen, K. Thornton, and N. P. Dasgupta, Operando video microscopy of Li plating and reintercalation on graphite anodes during fast charging, Journal of Materials Chemistry A **9**, 23522 (2021).

[48] Z. Ahmad, V. Venturi, H. Hafiz, and V. Viswanathan, Interfaces in Solid Electrolyte Interphase: Implications for Lithium-Ion Batteries, Journal of Physical Chemistry C **125**, 11301 (2021).

[49] N.Legrand, B.Knosp, P.Desprez, F.Lapicque, and L.S.Rae, Physical characterization of the charging process of a li-ion battery and prediction of li plating by electrochemical modelling, J. Power Sources **245**, 208 (2014).

[50] P. Bai, J. Li, F. Brushett, and M. Bazant, Transition of lithium growth mechanisms in liquid electrolytes, Energy Environ. Sci. **9**, 3221 (2016).

[51] J. Tan, M. Ye, and J. Shen, Tailoring uniform and ordered grain boundaries in the solid electrolyte interphase for dendrite-free lithium metal batteries, Materials Today Energy **22**, 100858 (2021).

[52] M. He, R. Guo, G. M. Hobold, H. Gao, and B. M. Gallant, The intrinsic behavior of lithium fluoride in solid electrolyte interphases on lithium, Proceedings of the National Academy of Sciences **117**, 73 (2020).

[53] H. Yildirim, A. Kinaci, M. K. Y. Chan, and J. P. Greeley, First-principles analysis of defect thermodynamics and ion transport in inorganic SEI compounds: LiF and NaF, ACS Applied Materials & Interfaces **7**, 18985 (2015).

[54] A. M. Colclasure, K. A. Smith, and R. J. Kee, Modeling detailed chemistry and transport for solid-electrolyte-interface (SEI) films in li–ion batteries, Electrochimica Acta **58**, 33 (2011).

[55] S. T. Lam, Q.-J. Li, R. Ballinger, C. Forsberg, and J. Li, Modeling lif and flibe molten salts with robust neural network interatomic potential, ACS Applied Materials & Interfaces **13**, 24582 (2021).

[56] A. Rodriguez, S. Lam, and M. Hu, Thermodynamic and Transport Properties of LiF and FLiBe Molten Salts with Deep Learning Potentials, ACS Applied Materials & Interfaces **13**, 55367– (2021).

[57] D. A. Cogswelland M. Z. Bazant, Coherency strain and the kinetics of phase separation in LiFePO4 nanoparticles, ACS Nano **6**, 2215 (2012).

[58] S. Carelliand W. G. Bessler, Prediction of Reversible Lithium Plating with a Pseudo-3D Lithium-Ion Battery Model, Journal of The Electrochemical Society **167**, 100515 (2020).

[59] S. Hein, T. Danner, and A. Latz, An Electrochemical Model of Lithium Plating and Stripping in Lithium Ion Batteries, ACS Applied Energy Materials **3**, 8519 (2020).

[60] K. Xu, Nonaqueous liquid electrolytes for lithium-based rechargeable batteries, Chemical Reviews **104**, 4303 (2004).

[61] A. Jana, D. R. Ely, and R. E. García, Dendrite-separator interactions in lithium-based batteries, Journal of Power Sources **275**, 912 (2015).

[62] K. Persson, Y. Hinuma, Y. S. Meng, A. Van Der Ven, and G. Ceder, Thermodynamic and kinetic properties of the Li-graphite system from first-principles calculations, Physical Review B - Condensed Matter and Materials Physics **82**, 125416 (2010).

[63] A. Bartol, R. E. García, D. R. Ely, and J. Guyer, The Virtual Kinetics of Materials Laboratory (2009).

[64] T. Cool, A. Bartol, M. Kasenga, K. Modi, and R. E. Garca, Gibbs: Phase equilibria and symbolic computation of thermodynamic properties, Calphad: Computer Coupling of Phase Diagrams and Thermochemistry **34**, 393 (2010).

[65] C. W. Monroe, C. Monroe, and J. Newman, Dendrite Growth in Lithium/Polymer Systems: A Propagation Model for Liquid Electrolytes under Galvanostatic Conditions, J. Electrochem. Soc. **150**, A1377 (2015).

[66] A. Jana, S. I. Woo, K. S. Vikrant, and R. E. García, Electrochemomechanics of lithium dendrite growth, Energy and Environmental Science **12**, 3595 (2019).

[67] K. S. Vikrant, H. Wang, A. Jana, H. Wang, and R. E. García, Flash sintering incubation kinetics, npj Computational Materials **6**, 98 (2020).

[68] H. Ge, T. Aoki, N. Ikeda, S. Suga, T. Isobe, Z. Li, Y. Tabuchi, and J. Zhang, Investigating Lithium Plating in Lithium-Ion Batteries at Low Temperatures Using Electrochemical Model with NMR Assisted Parameterization, Journal of The Electrochemical Society **164**, A1050 (2017).